

Winter thermohaline evolution along and below the Ross Ice Shelf

Received: 15 February 2024

Accepted: 21 November 2024

Published online: 04 December 2024

 Check for updates

Pierpaolo Falco¹, Naomi Krauzig¹, Pasquale Castagno², Angela Garzia^{1,3}, Riccardo Martellucci⁴, Yuri Cotroneo⁵, Daniela Flocco⁶, Milena Menna⁴, Annunziata Pirro⁴, Elena Mauri⁴, Francesco Memmola¹, Cosimo Solidoro⁴, Massimo Pacciaroni⁴, Giulio Notarstefano⁴, Giorgio Budillon⁵ & Enrico Zambianchi⁵ ✉

The Ross Ice Shelf floats above the southern sector of the Ross Sea and creates a cavity where critical ocean-ice interactions take place. Crucial processes occurring in this cavity include the formation of Ice Shelf Water, the coldest ocean water, and the intrusion of Antarctic Surface Water, the main driver of frontal and basal melting. During the winter, a polynya forms along the Ross Ice Shelf edge, producing a precursor to Antarctic Bottom Water known as High Salinity Shelf Water. Due to the difficulty of direct exploration of the Ross Ice Shelf in the winter, processes occurring there have been only hypothesized to date. Here we show thermohaline observations collected along the Ross Ice Shelf front from 2020 to 2023 using unconventionally programmed Argo floats. These measurements provide year-round observations of water column changes in and around the Ross Ice Shelf cavity, allowing to quantify production of High Salinity Shelf Water, ocean heat content and basal melt rates.

The Ross Ice Shelf (RIS) is the world's largest ice shelf. It plays a crucial role in stabilizing the West Antarctic Ice Sheet (WAIS) and in modulating its contribution to sea-level rise. With an area of ~480,000 km², the RIS buttresses ~11.6 m of potential contribution to global sea-level rise^{1,2}. Thus, this is an area of critical significance in a scenario of accelerating Antarctic Ice Sheet mass loss³.

Compared to other ice shelves of the WAIS, the RIS is currently considered to be in a relatively stable condition⁴ with changes of its rate of thickness relatively constant over the period of 1994–2012. On the other hand, evidence from geological records shows that the RIS has the potential to degenerate rapidly^{5–7}. Swath bathymetry data and sediment cores provide evidence for two episodes of ice-shelf collapse. Of these two episodes, the second (which occurred about 5000 years ago) affected a larger area of the RIS (about 280,000 km²),

impacting both the western and eastern sectors. Models and ice core data showed that the break-up of the RIS was caused by both atmospheric warming and warm water masses hitting the base of the ice shelf. At the end of this episode, the RIS acquired its current configuration⁷.

The predominant cause of these buttressing losses has been attributed to ocean-driven basal melting and calving, with calving representing the major loss mechanism for large and cold cavity ice shelves^{8–11}.

Both physical and biological responses to climate change have been observed in the Ross Sea, largely on decadal time scales. Air temperature values have been showing an increasing trend in the south, at the RIS edge, where the McMurdo station is located¹², whereas an opposite trend was observed in the northwestern margin¹³.

¹Dipartimento di Scienze della Vita e dell'Ambiente, Università Politecnica delle Marche and Consorzio Nazionale Interuniversitario per le Scienze del Mare, Ancona, Italy. ²Dipartimento di Scienze Matematiche e Informatiche, Scienze Fisiche e Scienze della Terra, Università degli Studi di Messina, Messina, Italy. ³Dipartimento di Ingegneria Civile, Edile e Ambientale, Sapienza Università di Roma, Roma, Italy. ⁴Istituto Nazionale di Oceanografia e di Geofisica Sperimentale – OGS, Sgonico (TS), Italy. ⁵Dipartimento di Scienze e Tecnologie, Università degli Studi di Napoli “Parthenope” and Consorzio Nazionale Interuniversitario per le Scienze del Mare, Napoli, Italy. ⁶Dipartimento di Scienze della Terra, dell'Ambiente e delle Risorse, Università degli Studi di Napoli “Federico II”, Napoli, Italy. ✉e-mail: enrico.zambianchi@uniparthenope.it

The average sea ice extent has been increasing since the early 1990s¹⁴, even though the number of ice-free days within the Ross Sea polynya are slightly increasing (see ref. 15 and references therein). Evidence of a decline in Ross Ice extent emerged in 2015¹⁶, perfectly timed with the reversal in sea ice extent observed around Antarctica¹⁷. The salinity field has shown a multidecadal freshening¹⁸ but after 2014 a significant rebound occurred¹⁹ related to the increase of ice production on the Ross Sea continental shelf²⁰. Climate projections for the Ross Sea indicate a stop in sea ice increase with effects on both physics and ecosystem functioning²¹, but there are still uncertainties. Regional simulations carried out using a coupled sea-ice circulation-ice shelf model²¹ based on expected atmospheric forcing variability (winds and air temperature) and forced by boundary-imposed freshening, foresee a summertime expansion of the polynya formed along the RIS (RIS polynya, hereafter RISp, also called in literature Ross Sea Polynya) and a contraction of the mixed layer depth.

New evidence has arisen from observations in the last decade for increased melting rates in parts of the RIS. In the RIS northwest sector (NWRIS) the measured melting rate was three times higher than in other RIS sectors during summer²². Data from the NWRIS are thus of great importance to evaluate the stability of the RIS front. The calving risk of large icebergs here can be higher and it has been observed that large icebergs calved from RIS²³ may limit the RIS polynya activity due to prolonged occupation of the area. Moreover, they represent a risk as they can alter the balance of other crucial areas of the Ross Sea, such as the Terra Nova Bay polynya area. There, in the past²⁴, large icebergs have impacted the Drygalski Ice Tongue, which is a key element for the formation of the coastal polynya and thus for the production of High Salinity Shelf Water (HSSW). Such events would decrease the production of shelf waters, precursor to the Antarctic Bottom Water (AABW).

Ice shelf melting is linked to three main density-driven circulation modes²⁵, defined according to the distinct intrusion of different water masses into the ice-shelf cavities: HSSW at freezing point (Mode 1), Circumpolar Deep Water (CDW, Mode 2), and seasonally-warmed Antarctic Surface Water (AASW), which intrudes during summer into cavities and leads to melting close to the ice shelf front (Mode 3). HSSW is formed in the two polynyas of the Ross Sea in winter due to brine release during sea ice formation and aided by the mechanical removal of ice induced by katabatic winds. HSSW enters the cavity close to the sea floor and, due to the high pressure, it carries heat to the grounding line, melting the RIS base. Cold and fresh melting water then mixes with the HSSW decreasing both its temperature and salinity. Ice Shelf Water (ISW) is then formed, and due to its lower density with respect to the HSSW, flows at depths of around 400 m. AASW (especially in summer) and mCDW are relatively warm waters, thus in principle they can melt the ice shelf once in contact with it. However, our data suggest that the role of mCDW in the melting of the RIS is negligible, if not completely absent, whereas the AASW plays a role in both the ablation of the RIS front and the basal melting. This is the reason why we focused our analysis on the intrusion of AASW into the cavity.

The three cavity circulation modes provide a primary control on the evolution of the Antarctic ice sheet^{11,22}, and yet direct observations of oceanographic conditions close to or inside the ice shelf cavities are extremely limited. Furthermore, the understanding of these processes is particularly difficult in winter, when sea ice restricts oceanographic operations. Shipboard and sea surface observations from satellites are also confined to summer periods and therefore we have a poor understanding of basic hydrographic changes, such as the seasonal progression of the thermohaline structure, of the heat content variability and of the ice-shelf basal melt rate.

Here we show the results obtained from the analysis of data collected by 7 Argo floats used in a non-conventional way, i.e., constrained at the edge of the RIS and in the RISp (see Fig. 1 and Methods). Data

describe the year-round thermohaline variability in key areas of the RIS front during 2020–2023. Invaluable under-ice measurements along and under the RIS and in the RISp during winter made it possible to follow seasonal changes of the main water mass vertical structure and provided first insights, from in-situ measurements, into the volume of HSSW produced in the RISp. These profiling floats also captured the outflow of the Ice Shelf Water (ISW), the coldest water mass in the world, and gave clear indications about the different exchange mechanisms between the ice shelf cavity and the open sea.

Wintertime evolution of the vertical structure of the water column along the RIS

Argo float observations revealed the seasonal changes of the water column along the RIS front, from 160° East to Ross Island (See Fig. 1 for deployment sites along with their definitions, and Fig. 2 for the yearly evolution of the conservative temperature, absolute salinity and freshwater content (FWC) profiles). In the wRIS, as summer was approaching, sea ice started to melt, producing a buoyant fresh and warm layer that came into contact with the RIS front wall and base. HSSW formed during the previous winter seasons was observed in the deep layer. The autumn profiles showed an increase in salinity due to sea ice formation and brine rejection that occurred as the atmosphere cooled and sea surface heat loss intensified. In the winter profiles, the vertical stratification observed in summer and autumn changed into one uniform layer of HSSW (a process observed only very recently in Terra Nova Bay, see ref. 26); at cRIS, HSSW was found from 200 m down to the bottom while Low Salinity Shelf Water (LSSW, as defined by ref. 27) was only present at eRIS. The FWC variability followed the seasonal cycle of the sea ice (see Fig. 2 and Supplementary Fig. 1d). The values peaked at about 10 cm in summer at the surface and decreased in winter, reaching a constant minimum value along the vertical. The FWC was zero at the depth where the salinity was equal to the reference value (see Methods).

The data from the two floats deployed in wRIS (float 1 and 2) show the formation of HSSW in a way never observed before. Figures 3a and 3b report data collected by float 2(wRIS): the isohaline of 34.79 g/kg (34.62 psu, the lower limit for HSSW salinity according to ref. 27), shoals rapidly beginning in mid-May. This was due to the salt released when sea ice formed, although the continued increase in salinity to values greater than 34.85 g/kg indicated HSSW production associated with polynya activity. Considering that the depth of the 34.79 g/kg isohaline was about 400 m before rising and it surfaced in less than 2 weeks, we estimate convection of the order of 1–2 m h⁻¹ (up to 2.5 m h⁻¹ in the most violent phase, see Supplementary Figs. 3–5). Over time, the isohaline of 34.92 g/kg also rose to the surface, the production of HSSW continued and finally both floats showed an almost homogeneous vertical distribution of salinity in October, with a salinity value even higher than 34.95 g/kg. The activity of the polynya stopped in early November when the summer regime began, and the isohalines sank.

Two floats (3 and 4) deployed in the RISp moved northward following a common path, eventually leaving the polynya area after mid-October. These floats captured the formation of HSSW but the salinity maximum was lower than in the wRIS (see Fig. 3c, d and Supplementary Fig. 1). The layer below the isohaline of 34.92 g/kg in the RISp was characterized by absolute salinity values close to and sometimes higher than 34.95 g/kg and conservative temperature < -1.85 °C. This was a layer of HSSW not produced in this area of the polynya, but near Ross Island (wRIS), where both temperature and salinity were the same as those observed in the deep layer. All three floats deployed here sampled this saltier HSSW layer, providing evidence that HSSW produced near Ross Island drifted eastward along the RIS front and most likely also flowed beneath the RIS cavity. This interpretation is an alternative to the one described in previous works in the early 2000s²⁸; which suggested that the HSSW present in this area and entering the

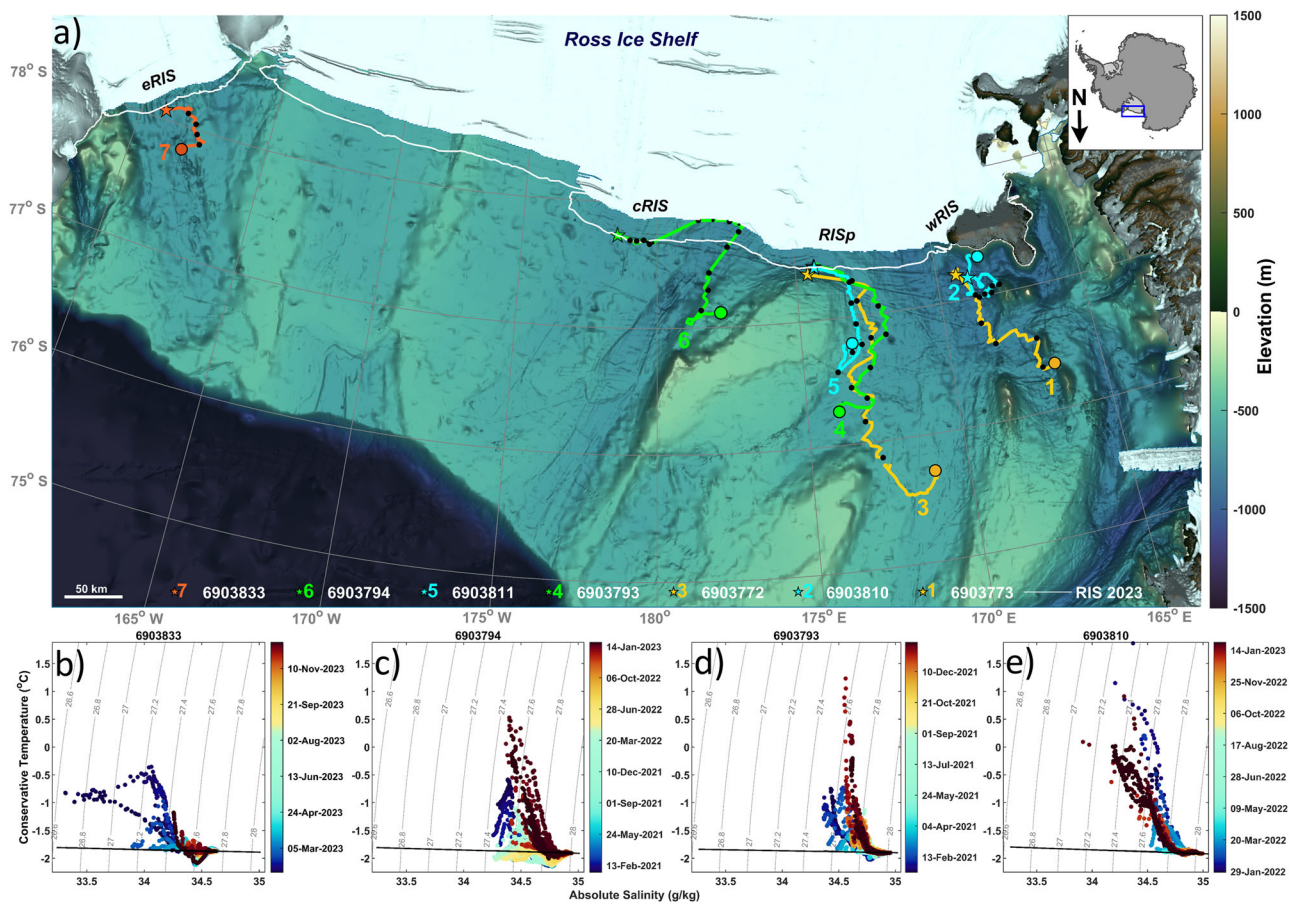


Fig. 1 | Map of the Ross Ice Shelf and summary of hydrological measurements. **a** Topographic map of the Ross Sea overlaid with the estimated trajectories (see Methods) of the Argo floats. The white line along the Ross Ice Shelf (RIS) represents the position of the ice shelf edge. In Supplementary Fig. 9 the positions of the RIS edge for the observation years are reported. On the trajectories, stars indicate the deployment positions and circles the recovery positions. The date of deployment and recovery position are reported in the Methods section. The black dots indicate

the estimated position every 2 months. **b–e** Comparison of water mass properties (conservative temperature and absolute salinity) measured by Argo floats along the RIS from East to West: easternmost (**b**, eRIS), central (**c**, cRIS), RIS polynya (**d**, RISp) and Ross Island (**e**, wRIS). Each salinity/temperature point is color-coded based on time. In Supplementary Fig. 2 the Temperature-Salinity diagrams obtained using practical salinity and potential temperature are shown, along with the the neutral density curves of 28.00 and 28.27 g/kg.

RIS cavity was produced in Terra Nova Bay polynya. Furthermore these findings agree with model results²⁹.

Float 7 was deployed in eRIS and is unique in its collection of measurements in the scarcely observed Eastern Ross Sea region (Fig. 3e, f). It is known to be characterized by LSSW²⁷ because the absence of polynyas prevents the formation of HSSW. Salinity measured by the float was always less than 34.79 g/kg, even at the bottom. In summer, the surface layer warmed up but was fresher and less thick than that in the western sector. This was very likely due to the influence of the glacial meltwater from the West Antarctic region, which enters the Ross Sea from the east. A signal of ISW appears at a depth of about 400–500 m from mid-February to the end of June. Its density was below the limit of shelf waters (SW, as reported by ref. 27) and could not even be considered as Modified Shelf Water (see again ref. 27). This water mass was characterized by very low temperature ($<-2^{\circ}\text{C}$) such as the ISW but with lower salinity than the shelf waters.

Observations beneath the RIS and HSSW production

Float 6 (cRIS, Fig. 4) was deployed at cRIS to monitor the ISW outflow and sampled three sub-areas: from January to November 2021 it remained in the deployment area; from early December 2021 to late July 2022 it was confined in the RIS cavity; then it left the RIS cavity and moved to the eastern edge of the RIS polynya. This float collected data during the 8 months it spent in the RIS cavity sampling T and S profiles

from the base of the RIS to the seafloor, capturing major water mass changes, heat transport beneath the RIS and basal melting of the shelf.

Starting in November 2021, we observed the beginning of the summer regime; satellite observations show that the sea ice concentration decreased along the coastline, allowing the ocean surface to be warmed. At this point the float was at the edge of the RIS and recorded an increase in water temperature and a decrease in salinity due to RIS and sea ice melting. A new, low-density layer then occupied the surface, pushing down the surface isopycnals (and isotherms) at, and even exceeding, the depth of the RIS draft. Beginning in December 2021, the surface isopycnals sank, creating the preconditioning (namely a favorable slope) for intrusion of warm AASW beneath the RIS. Here the float was trapped in this layer and recorded data from the RIS draft to the seafloor.

The intrusion of AASW under the RIS created the conditions for the melting of the basal ice and the formation of a fresh ISW layer in contact with the RIS. The FWC values here were like those observed in the surface layer in early summer when the sea ice was melting (Supplementary Fig. 1). ISW vertical plumes with an extent of more than 100 m were observed until the end of March, when the remnants of the AASW were at depths greater than the RIS draft. The float intercepted two more ISW plumes just before leaving the cavity. It is difficult to say whether these were earlier plumes that were now contracting, or whether they were formed by late melting of the base of the RIS.

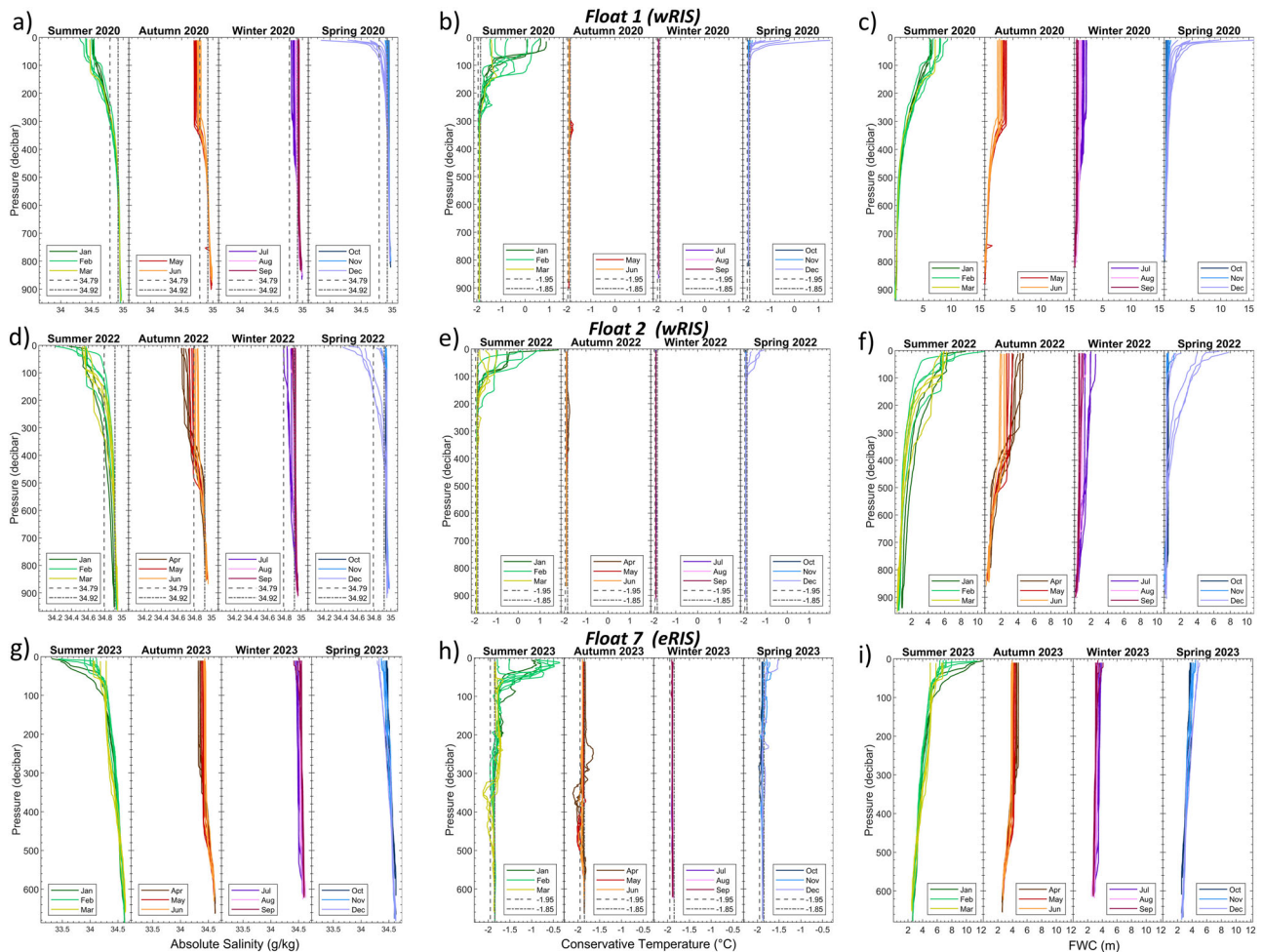


Fig. 2 | Time evolution of the vertical profile of hydrological properties along the Ross Ice Shelf. From left to right, absolute salinity, conservative temperature and Fresh Water Content (FWC) relative to a reference salinity of 34.8 psu profiles for float 1 (western Ross Ice Shelf wRIS, panels a–c), for float 2 (wRIS, panels d–f) and for float 7 (eastern Ross Ice Shelf eRIS, panels g–i). Profiles are grouped by seasons. Seasons are indicated on the top of the panels: summer refers to the

months of January, February and March; autumn to April, May and June; winter to July, August and September; spring to October, November and December. Profiles are color-coded based on the month. Dashed lines in the salinity plots represent the limits of the High Salinity Shelf Water (HSSW); dashed and dash-dotted lines in the temperature plots represent respectively the minimum temperature of Ice Shelf Water (ISW) and the temperature of the HSSW (values taken from ref. 27).

The relatively high temperature measured just before the first plume would suggest the second option.

Float 6 left the RIS cavity in July 2022, less than 100 km from the deployment site (see Fig. 1). Here, salinity values indicated an increase due to brine rejection but there was limited evidence of HSSW formation. The salinity maximum was about 34.85 g/kg from late August to the end of October and the water column was barely homogeneous in both salinity and temperature. We can consider this area as the easternmost limit for the polynya area producing HSSW.

The data collected by the floats thus provide us with information on the presence and extent of HSSW formation, allowing us to calculate the volume of HSSW formed in the RISp and the mass of salt produced (Supplementary Table 1, see Methods). We estimated the HSSW production to be between 0.1 and 0.4 Sv. These values are very close to the lower bound of the HSSW volume produced in Terra Nova Bay polynya^{24,30–32}. The related amount of salt produced in the RISp ranges between about 50 and 200 GT depending on the polynya area (see Methods and Supplementary Table 1).

Intrusion of warm surface water into the RIS cavity and basal melt rate

Here we report our assessment of how much heat is available to the AASW for ice shelf melting. The Argo floats deployed at the RISp and

cRIS described the intrusion of the warm summer AASW down to the base and into the cavity of the RIS, as shown in Fig. 5. The first casts taken by Float 3 (RISp) in January and early February (2020) measured a warm surface layer of AASW about 150 m thick, which later deepened, as did the surface isopycnal surfaces found at greater depths from mid-January 2020 (Fig. 5a, b). The downward tilt of the isopycnals was an effective way to push the warm summer AASW to a depth ultimately deeper than the RIS front base (wedge mechanism described by ref. 33). Therefore, the AASW could penetrate the cavity carrying heat and causing melting of the RIS base. As the surface layer cooled at the end of the summer, the entire water column tended to a homogeneous temperature structure and the transport of AASW downward stopped. However, warm water cores could be observed as late as April, beneath the surface layer that was cooling instead.

The way heat was transported beneath the RIS cavity was also well documented by floats 5 (RISp) and 6 (cRIS, Figs. 5c and 4c respectively). Float 6 described a long period of interaction of the warm AASW and the RIS draft. The vertical structure conducive to AASW transport in the cavity formed in early December. Interestingly, until this time the float is very close to the RIS front, moving parallel to it but outside of it. As soon as the melting of the RIS front produced sufficient AASW, with the consequent lowering and tilting of the surface isopycnals, the float entered the cavity.

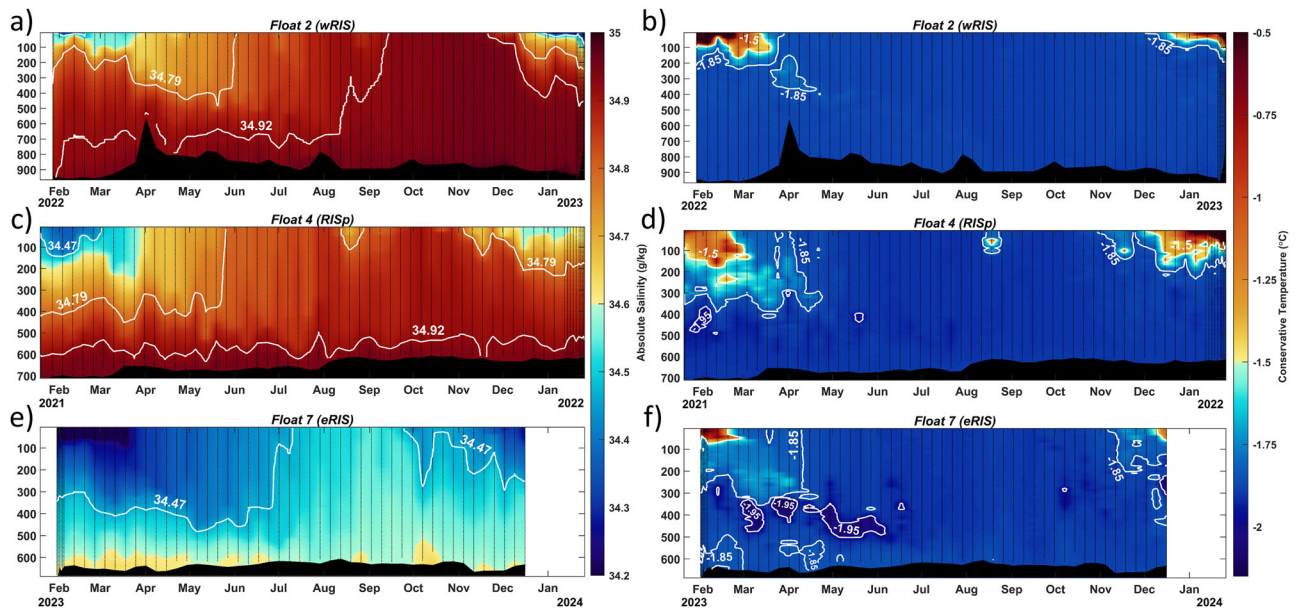


Fig. 3 | Time/depth distribution of hydrological properties along the Ross Ice Shelf. Time evolution of the vertical profile of absolute salinity (left panels) and conservative temperature (right panels) collected by float 2 (western Ross Ice Shelf

wRIS, panels a and b), float 4 (Ross Sea Polynya RISp, panels c and d), and float 7 (eastern Ross Ice Shelf eRIS, panels e and f). White areas indicate missing data. Each vertical black line indicates a float profile.

Float 5 (RISp), after the first profile, entered the RIS cavity in late January 2022 (Fig. 5c). At that time, the isopycnal of $\gamma_n = 28.2$ was at a depth of 300 m, and thus surface waters could move downward and into the cavity. As time went by, the float was pushed out of the cavity, intercepting the warm surface waters carried downward by the tilted isopycnals.

In terms of the amount of heat transported downward by the AASW, we estimated the ocean heat content (OHC) for each float (see Methods). Figures 5b, 5d, 4d and 5f show the time evolution of the OHC for floats 3, 5 (both in the RISp), 6 (cRIS), and 7 (eRIS) respectively. OHC peaked in the second half of February at both RISp and wRIS with values up to $9 \times 10^8 \text{ Jm}^{-2}$ over a thickness of 300 m for the westernmost floats. For the floats below the cavity, we found a value of $2 \times 10^8 \text{ Jm}^{-2}$ and a value slightly above $3 \times 10^8 \text{ Jm}^{-2}$ over a layer about 120 m depth for float 7 (eRIS). Looking at the surface layer occupied by AASW, there was a west-east gradient in OHC as well as a decrease in the thickness of the surface layer occupied by AASW.

Based on the OHC estimates, it is possible to obtain an estimate of the heat transported into the whole RIS cavity. Considering then the length of the RIS front and that the wedge effect decays northward over a distance from the RIS estimated by ref. 33 to be 100 km, we estimate that $3 \times 10^{19} \text{ J}$ are transported into the RIS cavity by the intrusion of summer heated AASW.

The differences in OHC measured from west to east impacted the ice shelf melt with a larger effect in the NWRIS. Using an average value of OHC of $5 \times 10^8 \text{ Jm}^{-2}$ for the NWRIS, $2 \times 10^8 \text{ Jm}^{-2}$ for the under ice shelf and eastern sector we found a basal melting rate (BMR, see Methods) of 1.6 and 0.6 m yr^{-1} respectively. In the NWRIS, the highest OHC ($9 \times 10^8 \text{ Jm}^{-2}$) would determine a BMR of about 3 m yr^{-1} . These values are in accordance with previous local and larger-scale estimates from in-situ and satellite data^{22,34,35}.

Implications and perspectives

Sea ice in polar regions is decreasing and the polar oceans are changing rapidly³⁶. The increased rate of ice loss from the Antarctic ice sheet in recent decades has increased the contribution to global sea-level rise³⁷. The extent of sea ice around Antarctica and also in the Ross Sea has decreased significantly in the last decade¹⁶, opening up a new scenario whose future consequences are difficult to understand.

Despite their importance, very high latitudes are still poorly explored, and the lack of observations not only limits the understanding and quantification of processes occurring here, but also the ability of models to make accurate predictions³⁸.

Argo floats deployed in a constrained mode are a promising approach for gathering continuous, in-situ observations of the polar regions. We have reported three years of data here, which is a period too short to characterize interannual variability and longer-term trends, but might form the basis for future studies on how, for example, changing atmospheric conditions may affect HSSW production in the RISp resulting in additional HSSW formation not captured by the weekly Argo float salinity measurements. The data collected provide insight into the amount of heat transported into the cavity as well as the lateral extent of production of HSSW in the RISp. It should be noted that we have estimated the volume of HSSW filling the part of the water column above the pre-existing HSSW layer. For future studies, it will be necessary to try and estimate the contribution of lateral advection, which may transport less saline water, resulting in an additional volume of HSSW to make the vertical column completely homogeneous. It is also important to understand which portion of the RISp is an active area of HSSW production. These data show that not all the open-water area visible in satellite imagery should be considered because only wRIS and RISp sectors clearly show formation of HSSW during winter. However, there is still uncertainty about how far north the production area extends. In this work, we have determined this boundary based on float profiles collected north of the RISp, thus providing at least a conservative estimate of HSSW production. This result highlights a fundamental difference between the two Ross Sea polynyas, most likely related to the different formation mechanisms. The TNB polynya is a typical mechanically forced polynya, whereas the RISp is more related to atmospheric weather systems affecting the southern sector of the Ross Sea³⁹. The RISp extent is also one of the possible causes of the much higher OHC values observed in wRIS than in the eRIS²²; changes in the number of ice-free days can be a factor influencing the warming of surface water and the amount of heat absorbed available for RIS front melting. We have also directly observed how the heat absorbed at the surface is transported into the cavity, which ultimately contributes to the basal melting.

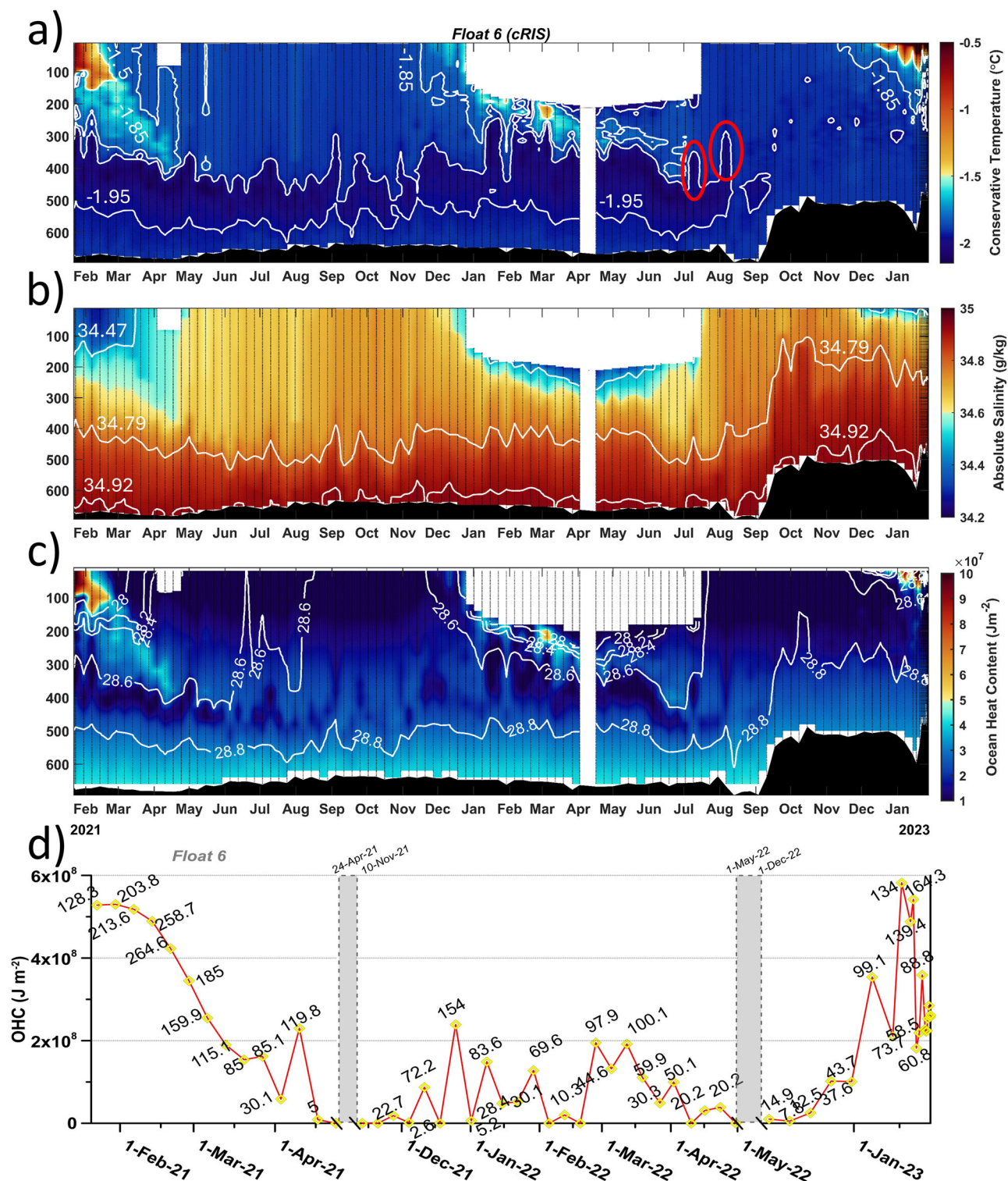


Fig. 4 | Time/depth distribution of hydrological properties under the Ross Ice Shelf. Time evolution of the vertical profile of absolute salinity (a), conservative temperature (b) and Ocean Heat Content (OHC) (c) for float 6. White areas indicate missing data. The white polygon in the surface layer from 0 to about 200 m indicates the presence of the Ross Ice Shelf. The surface white rectangle in April 2022 is

instead due to a gap in data collection. Each vertical black line in panels a–c indicates a float profile. Ice Shelf Water vertical plumes have been highlighted with red ovals in panel a. d Vertically integrated OHC for float 6. The numbers along the curves in panel d indicate the depth of the integration layer to obtain the OHC (see Methods).

Surface waters generally have a lower potential than mCDW to cause basal ice shelf melting, although they may be important locally. The flow of the shelf is particularly sensitive to thickness change near one such site, Ross Island. The RIS today has fewer pinning points⁷ than

in the Holocene, therefore it is more vulnerable to climate and oceanographic influences.

The BMRs calculated here are much lower than those observed in West Antarctic ice shelf cavities⁹ and much lower than those estimated

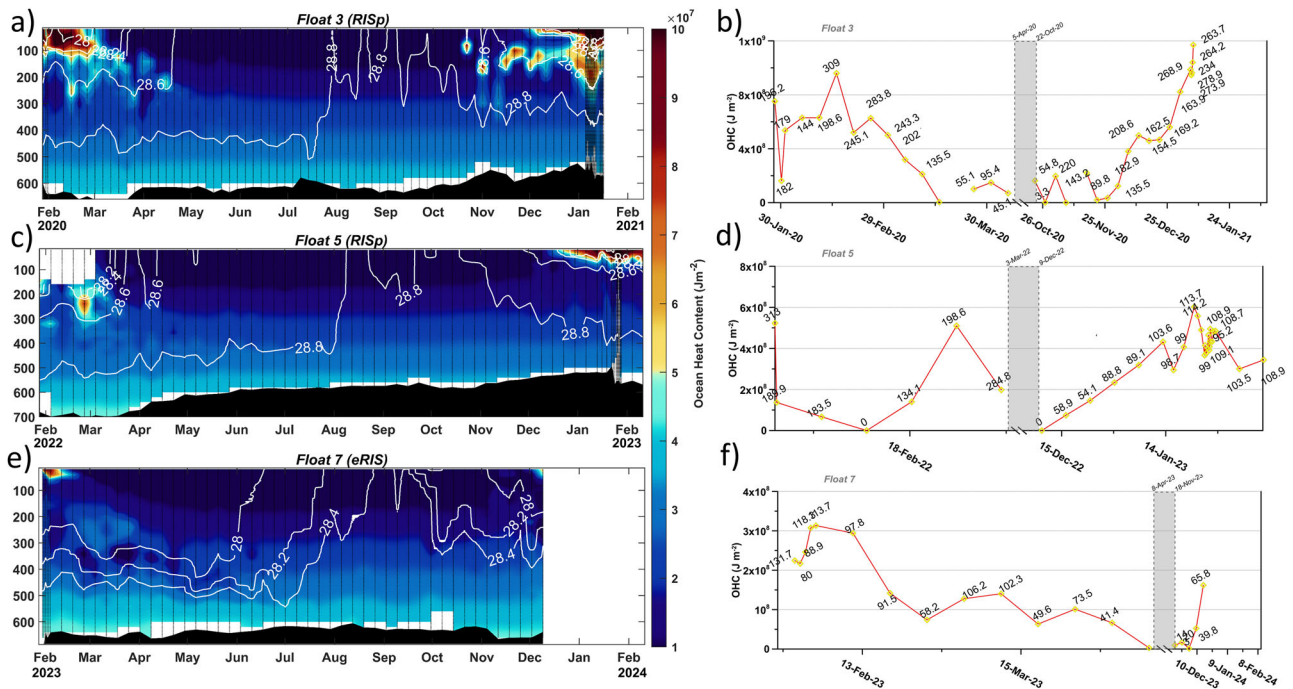


Fig. 5 | Time/depth distribution of ocean heat content along the Ross Ice Shelf. Time evolution of the vertical profile of the Ocean Heat Content (OHC, left panels) and of the vertically integrated OHC (right panels). The OHC goes to 0 during winter, thus the gray areas indicates all winters with OHC = 0, which we have chosen

not to show. The white curves in panels **a**, **c**, and **e** represent the neutral density isopycnals. The numbers along the curves in panels **b**, **d**, and **f** indicate the depth of the integration layer to obtain the OHC (see Methods). Each vertical black line in panels **a**, **c**, and **e** indicates a float profile.

at the time of the RIS collapse during the Holocene. The mCDWs are clearly not observed from the Argo floats we used for this work, and therefore one wonders if and how far the mCDWs actually reach the RIS. In conclusion, we believe the scientific community should consider the broad-scale implementation of constrained mode Argo floats across the entire Antarctic region: the ever-developing Argo float technology, along with some clever tweaking, paves the way to year-round thermohaline observations of the continental shelf areas in the polar regions, even in winter, in the presence of sea ice cover.

The unconventional use of Argo floats like the one described in this paper offers an opportunity to fill crucial data and knowledge gaps in polynyas near and under ice shelves, allowing for estimates of quantities crucial for the understanding of ice shelf stability, which may ultimately affect sea level rise.

Methods

Constrained Argo floats

Argo floats provide valuable data for a range of scientific and practical applications, including climate research, weather forecasting and ocean management (examples at <https://www.aoml.noaa.gov/argo/>). Thanks to an ice-sensing system, they can operate even when sea ice covers the ocean surface. Therefore, most Argo floats deployed in seasonal ice zones are now equipped with an ice-prevention function that analyses the measured temperature to estimate the probability of surface ice. A threshold temperature is set and if the float detects a temperature below the threshold during ascent, it will stop rising and sink back to the parking depth. As suggested by refs. 40,41, choosing a parking depth greater than the seafloor depth allows the floats to be parked on the seabed and thus minimize displacement between profiles. This clever method can greatly improve data collection in important areas of the Antarctic continental shelf, as floats remain confined near the deployment site. We used data from two floats deployed using this methodology in summer 2020, float 1 deployed 8/01/2020, recovered on 31/01/2021 after 89 cycles and float 3 deployed on 28/01/2020, recovered on 16/01/2021 after 99 cycles; two in

summer 2021, floats 4 deployed on 19/01/2021, recovered on 26/01/2022 after 61 cycles and float 6 deployed on 21/01/2021 recovered on 27/01/2023 after 121 cycles; two in summer 2022, float 2 deployed on 27/01/2022, recovered on 26/01/2023 after 66 cycles and float 5 deployed on 27/01/2022-04/03/2023 submerged again after 73 cycles; finally one in summer 2023, float 7 deployed on 29/01/2023, recovered on 31/01/2024 after 60 cycles. The time interval between each profile was set at 5 days for floats deployed in 2020 and 7 days for floats deployed thereafter.

During winter, when ice covers the sea surface, it is not possible to obtain satellite positions for under-ice profiles. Float trajectories were calculated as described below, in the section on georeferencing under ice. We always made sure to retrieve floats at the end of the second year's summer, i.e. before their estimated lifetime end, so as to avoid abandoning instruments in the Ross Sea, the world's largest marine protected area.

To obtain the Hovmöller diagrams in Figs. 3, 4a, c, e and 5a-c we used the The Climate Data Toolbox for MATLAB⁴². Interpolation is performed twice to create a gridded profile of each variable (CT or AS in our case). The first round interpolates the data from each Argo profile to equally-spaced depths. The second round interpolates horizontally to equally-spaced times.

Sea ice concentration and polynya area retrieval

We estimated the polynya area using the sea ice concentration dataset provided by the Meereis portal, implemented by the Alfred Wegener Institute. The portal provides daily Special Sensor Microwave Imager (SSM/I) data retrieved by measurements of the satellite radiometer Advanced Microwave Scanning Radiometer AMSR2 at a resolution of 6.25×6.25 km. Further details can be found on the MEEREIS website (<https://www.meereisportal.de/en/>).

Based on the above data and the observed formation of HSSW, we calculated the polynya extension in the area indicated by the black polygon in Supplementary Fig. 6. The off-shore limit of the polygon was chosen by considering the trajectory of the ARGO floats in the RISp

when HSSW production is observed. Following the trajectories northwards, floats in the RISp measured HSSW until the end of the winter period. Therefore, the limit represented by the point where the Argo floats detected HSSW formation can be considered the offshore limit of the formation area. The estimated period of polynya activity begins when the heat fluxes became negative at the end of summer and ends when they turned positive again at the end of winter (see Supplementary Fig. 7). This occurred approximately between March 15th and October 15th of each year considered (an example of how heat flux evolves over time and the relationship with the change in surface salinity is shown in Supplementary Fig. 7).

We identified the presence/absence of the polynya accounting for the grid cells where the sea ice concentration did not exceed the 50%, 75% and 90% threshold and then we compared the results⁴³ shown in Supplementary Table 1. The polynya area estimated in 2020 and 2022 shows a linear dependence on the threshold choice, while in 2021 this dependence is not as straightforward, due to the larger variability in the estimate as reflected by the higher standard deviation of the result.

We calculated the polynya area (*POLAREA*), using the following formulation

$$POLAREA = \sum_1^n A \times (1 - SIC) \quad (1)$$

Where n is the number of grid cells, A is the area of the grid cell and SIC is the sea ice concentration.

The analysis of the ice maps shows continuous activity of the polynya during winter. Periods of total surface coverage alternate with periods in which ice-free sectors are present, both in the central part of the study area and in an area very close to Ross Island (Supplementary Fig. 6). The largest area of the polynya was estimated as the sum of the mean extension and the standard deviation.

Volume of HSSW and mass of salt produced in the RIS polynya

First, we considered the time the surface layer water has absolute salinity >34.79 g/kg. We excluded from the calculation of the polynya extent the areas where HSSW production was not accomplished, as shown by the float observations. To calculate the volume of HSSW we used the relationship:

$$V = A_{polynya} \times h \quad (2)$$

where $A_{polynya}$ is the polynya surface extension calculated as described above (i.e., calculated across the March 15th - Oct 15th period) and h is the depth of the isohaline of absolute salinity 34.79 g/kg before the production of HSSW started. In Supplementary Table 2 we show, for each float and each area, the mean depth of the 34.79 g/kg isohaline estimated over the period starting in mid-February and ending when the isohaline outcropped at the surface (different for each float). Even with relatively few observations the depth of the isohaline is consistent over time and for each sector. See also Supplementary Figs. 3–5.

In this way we estimated the amount of HSSW filling the volume above the existing pre-winter deep layer of HSSW. To carry out this calculation we used the Argo floats that show the production of HSSW, namely the instruments in wRIS and RISp (see Figs. 2a, d and 3a, c). To obtain the rate of production we divided the volume by the length of the period of HSSW formation that, based on the timing of the shoaling and sinking of the 34.79 g/kg isohaline (e.g., Fig. 3a), spans from March 15th to October 15th.

To calculate the amount of salt produced by the whole polynya we used the relationship:

$$\text{Mass of salt} = (\rho Sh)A_{polynya} \quad (3)$$

where ρ is the mean density of the layer of depth h , h is the depth of the layer containing HSSW equal to 500 m (see Supplementary Table 2), S is the absolute salinity (g/kg). $A_{polynya}$ is the polynya surface extent. Results are shown in Supplementary Table 1.

Georeferencing under ice

The georeferencing of the under-ice Argo floats was based on a modified version of the terrain-following interpolation algorithm by ref. 44. Assuming barotropic potential vorticity conservation in a similar way to the methodology by ref. 45, this algorithm performs well in the vicinity of and along the continental slope where the currents mainly follow the isobaths.

The necessary bathymetric data were obtained from GEBCO's current gridded bathymetric data set, the GEBCO_2023 Grid (https://gebcoset.org/data_and_products/gridded_bathymetry_data/), which is a global terrain model for ocean and land, providing elevation data, in meters, on a 15 arc-second interval grid. Using the float measurements of pressure at the seabed and the known bathymetry, a reference depth was attributed to every position-lacking point, and the position was determined so as to minimize the difference between the local and the reference depth within a certain search range. The terrain-following trajectory was obtained by repeating this procedure for all position-lacking points. A revising procedure was carried out when the gap between the known position of the downstream endpoint and the last estimated point exceeded the selected search range. This involved defining acceptable interpolated positions based on a specific angle and carrying out a second iteration to determine the reference points as the centers for the search range.

Here, we utilized the modified version of Coriolis (<https://www.coriolis.eu.org/Observing-the-Ocean/ARGO>) which is freely provided through the EuroArgo github depository (<https://github.com/euroargodev/Coriolis-under-ice-positioning/commits?author=catsch>). This algorithm differs from the original one by ref. 46 in two main ways. Firstly, it implements an additional backward revision which enables the detection of eligible positions forward and backward for shallow bathymetry, avoiding dead ends in the isobath. Secondly, it takes into account in-situ data (e.g., the average drift depth, the maximum depth of the profile and the grounded flag) from each float to constrain the algorithm.

Ocean heat, fresh water content, basal melt rate calculations and heat fluxes data

We calculated the Ocean Heat Content (OHC) using temperature and density data provided by the Argo floats. The OHC over the area of study was calculated considering the difference between the in-situ temperature and the in-situ freezing temperature⁴⁶ calculated from salinity and pressure.

$$OHC = C_p \int_{h_1}^{h_2} \rho(z) [T(z) - T_0(z)] dz \quad (4)$$

where C_p is the specific heat capacity of sea water, h_1 and h_2 are the depths of the two temperature peaks, $\rho(z)$ is the sea water density and $T(z)$ and $T_0(z)$ are the sea water temperature and freezing point at depth z .

For the estimate of the total heat transported by AASW into the cavity we calculated the total volume of the layer occupied by the AASW. This volume is calculated from the length of the RIS front (about 600 km); the width of the AASW (distance from the RIS front to the off-shore limit) estimated at 100 km by ref. 33; the depth of the AASW layer at 100 m. Afterwards, we multiplied the volume by the average value of the OHC (about $5 \times 10^8 \text{ Jm}^{-2}$).

The average basal melt rate (BMR) was estimated considering the heat content of the warm surface water advected under the RIS cavity

($T > -1.75^\circ\text{C}$). The amount of basal melt was calculated as follows:

$$BMR = \frac{OHC}{L_f \rho_i} \quad (5)$$

where OHC is the Ocean Heat Content calculated as described above. The maximum heat content values were divided by the latent heat of fusion ($L_f = 3.34 \times 10^5 \text{ J/kg}$) and the ice density ($\rho_i = 918 \text{ kg/m}^3$), considering the values from ref. 47.

The Fresh Water Content (FWC), following ref. 48, can be calculated for each Argo profile as:

$$FWC = \int_{z_{lim}}^{surf} \frac{S_{Ref} - S(z)}{S_{Ref}} dz \quad (6)$$

where S_{ref} and S are, respectively, the reference salinity (chosen in our study as 34.8 psu) and in-situ salinity; z_{lim} is the depth at which $S(z)$ is equal to S_{ref} .

Daily surface heat fluxes data (mean surface net short-wave radiation flux, mean surface net long-wave radiation flux, mean surface latent heat flux, mean surface sensible heat flux) for the Ross Sea area were extracted from the Copernicus Climate ERA5 hourly data on single levels from 1979 to present dataset (Copernicus climate data store, <https://doi.org/10.24381/cds.adbb2d47>).

Data availability

All utilized Argo float data were made available by Argo-Italy and can be downloaded through their website <http://maosapi.inogs.it/#/data>. Sea ice concentration data were obtained from the AWI Meereis Portal (<https://www.meereisportal.de>; grant: REKLIM-2013-04). BedMachine v3 data (<https://doi.org/10.5067/FPSUOVIMWUB6>) are provided through the National Snow and Ice Data Center (<https://nsidc.org/data/nsidc-0756/versions/3>) and stem from ref. 49. IceLines data (<https://doi.org/10.15489/btc4qu75gr92>), published with the CC BY 4.0 licence, are freely available through the German Aerospace Center (<https://geoservice.dlr.de/data-assets/btc4qu75gr92.html>) and the utilized estimations for the Ross Ice Shelf edge from 2020 to 2023 were manually processed and edited by Dr. Celia Baumhoer (Celia.Baumhoer@dlr.de). The manually edited data can be provided upon personal request and additional information can be found in refs. 50,51.

Code availability

MATLAB scripts used for the analyses described in this study can be obtained from the corresponding author on request.

References

- Reese, R., Gudmundsson, G. H., Levermann, A. & Winkelmann, R. The far reach of ice-shelf thinning in Antarctica. *Nat. Clim. Change* **8**, 53–57 (2018).
- Tinto, K. J. et al. Ross Ice Shelf response to climate driven by the tectonic imprint on seafloor bathymetry. *Nat. Geosci.* **12**, 441–449 (2019).
- Stevens, C. et al. Ocean mixing and heat transport processes observed under the Ross Ice Shelf control its basal melting. *Proc. Natl Acad. Sci.* **117**, 16799–16804 (2020).
- Paolo, F. S., Fricker, H. A. & Padman, L. Volume loss from Antarctic ice shelves is accelerating. *Science* **348**, 327–331 (2015).
- Naish, T. et al. Obliquity-paced Pliocene West Antarctic ice sheet oscillations. *Nature* **458**, 322–328 (2009).
- Anderson, J. B. et al. Ross Sea paleo-ice sheet drainage and deglacial history during and since the LGM. *Quat. Sci. Rev.* **100**, 31–54 (2014).
- Yokoyama, Y. et al. Widespread collapse of the Ross Ice Shelf during the late Holocene. *Proc. Natl Acad. Sci.* **113**, 2354–2359 (2016).
- Liu, Y. et al. Ocean-driven thinning enhances iceberg calving and retreat of Antarctic ice shelves. *Proc. Natl Acad. Sci.* **112**, 3263–3268 (2015).
- Rignot, E., Jacobs, S., Mouginot, J. & Scheuchl, B. Ice-shelf melting around Antarctica. *Science* **341**, 266–270 (2013).
- Rignot, E. et al. Four decades of Antarctic Ice Sheet mass balance from 1979–2017. *Proc. Natl Acad. Sci.* **116**, 1095–1103 (2019).
- Adusumilli, S., Fricker, H. A., Medley, B., Padman, L. & Siegfried, M. R. Interannual variations in meltwater input to the Southern Ocean from Antarctic ice shelves. *Nat. Geosci.* **13**, 616–620 (2020).
- LaRue, M. A. et al. Climate Change Winners: Receding Ice Fields Facilitate Colony Expansion and Altered Dynamics in an Adélie Penguin Metapopulation. *PLOS ONE* **8**, e60568 (2013).
- Sinclair, K. E., Bertler, N. A. N. & van Ommen, T. D. Twentieth-Century Surface Temperature Trends in the Western Ross Sea, Antarctica: Evidence from a High-Resolution Ice Core. *J. Clim.* **25**, 3629–3636 (2012).
- Stammerjohn, S. E., Martinson, D. G., Smith, R. C., Yuan, X. & Rind, D. Trends in Antarctic annual sea ice retreat and advance and their relation to El Niño–Southern Oscillation and Southern Annular Mode variability. *J. Geophys. Res.* **113**, C03S90 (2008).
- Schine, C. M., van Dijken, G. & Arrigo, K. R. Spatial analysis of trends in primary production and relationship with large-scale climate variability in the Ross Sea, Antarctica (1997–2013). *J. Geophys. Res. Oceans* **121**, 368–386 (2016).
- Swathi, M., Kumar, A. & Mohan, R. Spatiotemporal evolution of sea ice and its teleconnections with large-scale climate indices over Antarctica. *Mar. Pollut. Bull.* **188**, 114634 (2023).
- Purich, A. & Doddridge, E. W. Record low Antarctic sea ice coverage indicates a new sea ice state. *Comm. Earth Environ.* **4**, 314 (2023).
- Jacobs, S. S., Giulivi, C. F. & Dutrieux, P. Persistent Ross Sea freshening from imbalance West Antarctic ice shelf melting. *J. Geophys. Res.: Oceans* **127**, e2021JC017808 (2022).
- Castagno, P. et al. Rebound of shelf water salinity in the Ross Sea. *Nat. Commun.* **10**, 5441 (2019).
- Silvano, A. et al. Recent recovery of Antarctic Bottom Water formation in the Ross Sea driven by climate anomalies. *Nat. Geosci.* **13**, 780–786 (2020).
- Smith, W. O. Jr., Ainley, D. G., Arrigo, K. R. & Dinniman, M. S. The oceanography and ecology of the Ross Sea. *Ann. Rev. Mar. Sci.* **6**, 469–487 (2014).
- Stewart, C. L., Christoffersen, P., Nicholls, K. W., Williams, M. J. & Dowdeswell, J. A. Basal melting of Ross Ice Shelf from solar heat absorption in an ice-front polynya. *Nat. Geosci.* **12**, 435–440 (2019).
- Depoorter, M. A. et al. Calving fluxes and basal melt rates of Antarctic ice shelves. *Nature* **502**, 89–92 (2013).
- Robinson, N. J. & Williams, M. J. M. Iceberg-induced changes to polynya operation and regional oceanography in the southern Ross Sea, Antarctica, from in situ observations. *Ant. Sci.* **24**, 514–526 (2012).
- Jacobs, S. S., Helmer, H. H., Doake, C. S., Jenkins, A. & Frolich, R. M. Melting of ice shelves and the mass balance of Antarctica. *J. Glaciol.* **38**, 375–387 (1992).
- Miller, U. et al. High Salinity Shelf Water production in Terra Nova Bay, Ross Sea from high-resolution near-surface salinity observations. *Nat. Commun.* **15**, 373 (2024).
- Orsi, A. J. & Wiederwohl, C. L. A recount of Ross Sea waters. *Deep Sea Res. II* **56**, 778–795 (2009).
- Budillon, G. et al. An optimum multiparameter mixing analysis of the shelf waters in the Ross Sea. *Ant. Sci.* **15**, 105–118 (2003).
- Jendersie, S., Williams, M. J., Langhorne, P. J. & Robertson, R. The density-driven winter intensification of the Ross Sea circulation. *J. Geophys. Res. Oceans* **123**, 7702–7724 (2018).
- Kurtz, D. D. & Bromwich, D. H. Katabatic wind forcing of the Terra Nova Bay polynya. *J. Geophys. Res.* **89**, 3561–3572 (1984).

31. Fusco, G., Budillon, G. & Spezie, G. Surface heat fluxes and thermohaline variability in the Ross Sea and in Terra Nova Bay polynya. *Cont. Shelf Res.* **29**, 1887–1895 (2009).
32. Rusciano, E., Budillon, G., Fusco, G. & Spezie, G. Evidence of atmosphere–sea ice–ocean coupling in the Terra Nova Bay polynya (Ross Sea–Antarctica). *Cont. Shelf Res.* **61–62**, 112–124 (2013).
33. Malyarenko, A., Robinson, N. J., Williams, M. J. M. & Langhorne, P. J. A Wedge Mechanism for Summer Surface Water Inflow into the Ross Ice Shelf Cavity. *J. Geophys. Res.* **124**, 1196–1214 (2019).
34. Silvano, A., Rintoul, S. R. & Herraiz-Borreguero, L. Ocean-Ice Shelf Interaction in East Antarctica. *Oceanography* **29**, 130–143 (2016).
35. Arzeno, I. B. et al. Ocean variability contributing to basal melt rate near the ice front of Ross Ice Shelf, Antarctica. *J. Geophys. Res.* **119**, 4214–4423 (2014).
36. Meredith, M. et al. Polar regions. In *IPCC special report on the ocean and cryosphere in a changing climate*. 1st ed. (Cambridge, UK Cambridge University Press, 2019)
37. Naughten, K. A., Holland, P. R. & De Rydt, J. Unavoidable future increase in West Antarctic ice-shelf melting over the twenty-first century. *Nat. Clim. Change* **13**, 1222–1228 (2023).
38. Smith, G. C. et al. Polar Ocean Observations: A critical gap in the observing system and its effect on the environmental predictions from hours to seasons. *Front. Mar. Sci.* **6**, 429 (2019).
39. Morales Maqueda, M. A., Willmott, A. J. & Biggs, N. R. T. Polynya dynamics: A review of observations and modeling. *Rev. Geophys.* **42**, RG1004 (2004).
40. Porter, D. F. et al. Evolution of the Seasonal Surface Mixed Layer of the Ross Sea, Antarctica, Observed With Autonomous Profiling Floats. *J. Geophys. Res.* **124**, 4934–4953 (2019).
41. Wallace, L. O., Van Wijk, E. M., Rintoul, S. R. & Hally, B. Bathymetry-Constrained Navigation of Argo Floats Under Sea Ice on the Antarctic Continental Shelf. *Geophys. Res. Lett.* **47**, e2020GL087019 (2020).
42. Greene, C. A. et al. The Climate Data Toolbox for MATLAB. *Geochem. Geophys. Geosyst.* **20**, 3774–3781 (2019).
43. Portela, E. et al. Seasonal Transformation and Spatial Variability of Water Masses Within MacKenzie Polynya, Prydz Bay. *J. Geophys. Res.* **126**, e2021JC017748 (2021).
44. Yamazaki, K., Aoki, S., Shimada, K., Kobayashi, T. & Kitade, Y. Structure of the subpolar gyre in the Australian-Antarctic Basin derived from Argo floats. *J. Geophys. Res.* **125**, e2019JC015406 (2020).
45. Chamberlain, P. M. et al. Observing the ice-covered Weddell Gyre with profiling floats: Position uncertainties and correlation statistics. *J. Geophys. Res.* **123**, 8383–8410 (2018).
46. Dotto, T. S. et al. Control of the Oceanic Heat Content of the Getz-Dotson Trough, Antarctica, by the Amundsen Sea Low. *J. Geophys. Res.* **125**, e2020JC016113 (2020).
47. Holland, D. M. & Jenkins, A. Modeling Thermodynamic Ice–Ocean Interactions at the Base of an Ice Shelf. *J. Phys. Oceano.* **29**, 1787–1800 (1999).
48. McPhee, M. G., Proshutinsky, A., Morison, J. H., Steele, M. & Alkire, M. B. Rapid change in freshwater content of the Arctic Ocean. *Geophys. Res. Lett.* **36**, 10 (2009).
49. Morlighem, M. et al. BedMachine v3: Complete bed topography and ocean bathymetry mapping of Greenland from multi-beam echo sounding combined with mass conservation. *Geophys. Res. Lett.* **44**, 11.051–11.061 (2017).
50. Baumhoer, C. IceLines – Ice Shelf and Glacier Front Time Series. EOC GeoService <https://doi.org/10.15489/btc4qu75gr92> (2022).
51. Baumhoer, C. A., Dietz, A. J., Heidler, K. & Kuenzer, C. IceLines – A new data set of Antarctic ice shelf front positions. *Sci. Data* **10**, 138 (2023).
52. Greene, C. A., Gwyther, D. E. & Blankenship, D. D. Antarctic Mapping Tools for Matlab. *Comp. Geosci.* **104**, 151–157 (2017).

Acknowledgements

This research was supported by the Italian Ministry of University and Research as part of the Argo-Italy program (EM) and of the Italian National Program for Antarctic Research (ESTRO PNRA18_00258 project EZ; ACCESS PNRA19_00032 project YC) and the Marine Observatory of the Ross Sea (MORSea OSS-13 project GB). BedMachine data from Morlighem et al. (<https://nsidc.org/data/nsidc-0756/versions/3>). IceLines data are freely available through the German Aerospace Center (DLR) and the utilized estimations for the Ross Ice Shelf edge from 2020 to 2023 were manually processed and edited by Dr. Celia Baumhoer (Celia.Baumhoer@dlr.de). These data can be provided upon personal request. The authors would like to thank Dr. Celia Baumhoer for providing the manually edited IceLines data of the Ross Ice Shelf. In addition, we acknowledge the use of the BedMachine toolbox and the Antarctic Mapping Tools⁵². We are grateful to Teresa A. Hann for her help in reviewing the manuscript.

Author contributions

P.F., P.C. and E.Z. planned the experiment. P.F., E.Z., and N.K. wrote the manuscript. N.K., A.G., R.M., C.S. and D.F. analyzed the data and prepared the figures. P.C., Y.C., D.F., E.M., F.M., M.M., A.P. contributed to the paper organization and to the critical analysis of the results. P.F., P.C., N.K., M.P., Y.C. and G.N. contributed to the deployment and recovery of the Argo Floats in the Ross Sea. G.B. helped with project management. All Authors reviewed and edited the manuscript.

Competing interests

The authors declare no competing interests.

Additional information

Supplementary information The online version contains supplementary material available at <https://doi.org/10.1038/s41467-024-54751-8>.

Correspondence and requests for materials should be addressed to Enrico Zambianchi.

Peer review information *Nature Communications* thanks Una Miller and the other, anonymous, reviewer for their contribution to the peer review of this work. A peer review file is available.

Reprints and permissions information is available at <http://www.nature.com/reprints>

Publisher's note Springer Nature remains neutral with regard to jurisdictional claims in published maps and institutional affiliations.

Open Access This article is licensed under a Creative Commons Attribution-NonCommercial-NoDerivatives 4.0 International License, which permits any non-commercial use, sharing, distribution and reproduction in any medium or format, as long as you give appropriate credit to the original author(s) and the source, provide a link to the Creative Commons licence, and indicate if you modified the licensed material. You do not have permission under this licence to share adapted material derived from this article or parts of it. The images or other third party material in this article are included in the article's Creative Commons licence, unless indicated otherwise in a credit line to the material. If material is not included in the article's Creative Commons licence and your intended use is not permitted by statutory regulation or exceeds the permitted use, you will need to obtain permission directly from the copyright holder. To view a copy of this licence, visit <http://creativecommons.org/licenses/by-nc-nd/4.0/>.

© The Author(s) 2024